ARL-TR-9608 ● Oct 2022

DEVCOM ARMY RESEARCH LABORATORY

Computer Vision Quantification of Complex Fracture

by Logan Shannahan and Phillip Jannotti

NOTICES

Disclaimers

The findings in this report are not to be construed as an official Department of the Army position unless so designated by other authorized documents.

Citation of manufacturer's or trade names does not constitute an official endorsement or approval of the use thereof.

Destroy this report when it is no longer needed. Do not return it to the originator.

ARL-TR-9608 ● OCT 2022

Computer Vision Quantification of Complex Fracture

Logan Shannahan and Phillip Jannotti
DEVCOM Army Research Laboratory

REPORT DOCUMENTATION PAGE

Form Approved
OMB No. 0704-0188

1. REPORT DATE *(DD-MM-YYYY)*	2. REPORT TYPE	3. DATES COVERED (From - To)
October 2022	Technical Report	October 2021–September 2022

4. TITLE AND SUBTITLE
Computer Vision Quantification of Complex Fracture

5a. CONTRACT NUMBER

5b. GRANT NUMBER

5c. PROGRAM ELEMENT NUMBER

6. AUTHOR(S)
Logan Shannahan and Phillip Jannotti

5d. PROJECT NUMBER

5e. TASK NUMBER

5f. WORK UNIT NUMBER

7. PERFORMING ORGANIZATION NAME(S) AND ADDRESS(ES)
DEVCOM Army Research Laboratory
ATTN: FCDD-RLW-TB
Aberdeen Proving Ground, MD 21005

8. PERFORMING ORGANIZATION REPORT NUMBER
ARL-TR-9608

9. SPONSORING/MONITORING AGENCY NAME(S) AND ADDRESS(ES)

10. SPONSOR/MONITOR'S ACRONYM(S)

11. SPONSOR/MONITOR'S REPORT NUMBER(S)

12. DISTRIBUTION/AVAILABILITY STATEMENT
Approved for public release: distribution unlimited.

13. SUPPLEMENTARY NOTES
ORCID IDs: P Jannotti, 0000-0002-5015-5866

14. ABSTRACT
Ballistic impact and other Army-relevant impact conditions result in complex multicrack fractures. These fractures are typically analyzed via qualitative analysis of postmortem and high-speed in-situ photography. Computer vision techniques to extract and digitize cracks are demonstrated, and the resulting features are analyzed statistically to both extract underlying physics and allow quantitative comparison between experiments and simulations. Two case studies applying the technique are presented: in-situ X-ray imagery of boron carbide ceramic under ballistic impact and simulations modeling fracture in skull cap.

15. SUBJECT TERMS
dynamic, fracture, X-ray, Terminal Effects, multicrack

16. SECURITY CLASSIFICATION OF:			17. LIMITATION OF ABSTRACT	18. NUMBER OF PAGES	19a. NAME OF RESPONSIBLE PERSON
a. REPORT	b. ABSTRACT	c. THIS PAGE			Logan Shannahan
Unclassified	Unclassified	Unclassified	UU	23	19b. TELEPHONE NUMBER (Include area code) (410) 278-1145

Standard Form 298 (Rev. 8/98)
Prescribed by ANSI Std. Z39.18

Contents

List of Figures iv

List of Tables v

1. Introduction 1

2. Methods, Assumptions, and Procedures 2

2.1 X-ray Fracture 2

2.2 Computer Vision Detection of Fracture 3

3. Results and Discussion 8

3.1 X-ray Fracture in Boron Carbide 8

3.2 Randomized Behind-Helmet Blunt Trauma Simulations 11

4. Conclusions 13

5. References 14

List of Symbols, Abbreviations, and Acronyms 15

Distribution List 16

List of Figures

Fig. 1 Experimental setup for instrumented ballistic testing. (Top) Shown is one of the high-precision launchers capable of achieving 2.5 km/s for a single-stage powder gun. (Bottom) Schematic of the setup and data collected for phase contrast imaging experiments, which utilize optical triggers to synchronize X-ray pulses and instrumentation. Full motion control of the target and gun is possible with high linear and angular resolution for precise sample alignment (10 μm and 1 mrad, respectively). 3

Fig. 2 (Left) The raw X-ray fracture image in boron carbide prior to any processing. (Right) The complement of the initial image after filtering out white noise. 4

Fig. 3 (Left) The image used to determine background illumination differences. Note that the image is darker toward the left and lighter toward the right. (Right) The main image after the subtraction of the background illumination. 5

Fig. 4 (Top left) The initial binarized image is shown. Note both the detected cracks and extraneous noise. (Top right) The first filter step removes some of the noise but is not sufficient. (Bottom left) The second filter strep removes all but the largest noise features while leaving the cracks intact. (Bottom right) The final binarized image is overlaid on the original image. 6

Fig. 5 (Top) The skeletonized image is shown. While cracks are mostly successfully detected, there remains some error, especially in the form of branched loops. (Bottom) A skeletonized version of the binarized image after a hole-filling operation is shown. This better captures the branching behavior at the cost of less accurate crack tracking, as can be seen near the impact site to the left. 7

Fig. 6 All eight frames of the X-ray imagery of the fracture response of boron carbide 8

Fig. 7 (Top) The distribution of crack length is shown. Cracks under 10 μm are removed to filter noise. Most cracks are between 10 and 150 μm in length, with one outlier of approximately 600 μm. (Middle) The orientation of each crack is shown. The spread is relatively even, corresponding with the visually observed radial spread of fracture from the impact location. (Bottom) A histogram of the calculated tortuosity is shown. As most of the cracks in the analyzed image are straight, the tortuosity clusters around a value of one. 9

Fig. 8 Simulations of fracture in a model skull are overlayed with detected cracks (white lines). The blue elements are undamaged, while other colors represent failed elements that make up simulated cracks. The top-right image uses the initial simulation parameters, while the remainder use randomized element properties to mimic the variability of human bone 12

List of Tables

Table 1 Collected statistics 10
Table 2 Skullcap fracture simulations..... 13

1. Introduction

The extraction and quantification of fracture information is one of the more challenging problems in experimental mechanics. The simplest methods of analysis use postmortem measurement of length or crack tip opening. However, this has the inherent drawback of only capturing the end state of the fracture, which can be misleading or even useless in the case of a sample tested to destruction. The methods of caustics and photoelasticity provide in-situ optical measurements of fracture toughness but require transparent or reflective materials for caustics and birefringent materials or coatings for photoelasticity (Dally and Kobayashi 1980; Zehnder and Rosakis 1990). Kirugulige et al. (2007) and Yoneyama et al. (2006) utilized advancements in modern high-speed photography and digital image correlation (DIC) techniques to develop a methodology for the measurement of stress intensity factors in isotropic materials. This method functions by the measurement of local displacements around the crack tip through DIC, which are then used to fit the theoretical asymptotic solution for the stress field around a crack tip. Shannahan et al. further expanded this technique to mixed-mode fracture in complex anisotropic materials such as bone and MAX phase nanocarbides (Shannahan et al. 2015, 2017; Shannahan 2017). Periasamy and Tippur (2012) also continued to develop the concept of fracture measurement through capture of local stresses with the digital gradient sensing method, which measures angular deflections around the crack tip instead of displacement for greater sensitivity.

While all of these methodologies are useful and provide otherwise unavailable information on the fracture toughness of a stationary or propagating crack, they all require a single crack tip that is not interacting with other cracks or the sample boundaries. This makes them unsuitable for the complex multicrack fractures resulting from ballistic impacts and other Army-relevant situations. In these conditions, the inherent difficulty of extracting quantifiable data based on the physics of the fracture means that most analyses of postmortem or in-situ fractures of this kind are purely qualitative. It is often considered sufficient to compare experiments through notable features and a high-level overview of the fracture pattern, such as ring cracks versus conical cracks radiating from the impact or branching and twisting cracks versus straight. However, with modern high-quality, high-speed video and computer vision techniques, there is the opportunity to do more.

This report describes a computer vision–based methodology to detect cracks and extract a statistical breakdown of a complex fracture. This method is material and loading agnostic in that it functions as long as the cracks are sufficiently visible against background contrast and noise. Once detected and digitized, the image is

analyzed, and a variety of statistics are extracted to quantitatively describe the fracture pattern. These statistics allow for a direct quantitative comparison between both series of experimental data and simulation data. Two case studies are used to present this method: one examining in-situ X-ray fracture data in boron carbide and one analyzing a simulation of skull fracture resulting from behind-helmet blunt trauma (Alexander et al. 2021).

2. Methods, Assumptions, and Procedures

2.1 X-ray Fracture

Small-scale terminal ballistic experiments were conducted at the Dynamic Compression Sector of the Advanced Photon Source (APS) at Argonne National Laboratory, as shown in Fig. 1. The experiment consisted of a pure copper rod (3-mm length and 0.6-mm diameter) impacting commercial-grade boron carbide (Coorstek PAD-B_4C; 8-mm width and height and 7 mm in the impact direction). The projectile was launched using a polycarbonate sabot in a single-stage smoothbore 0.50-cal. powder gun. Incipient deformation and fracture were captured using propagation-based phase contrast imaging (PCI) at a characteristic time interval of 153.4 ns in the initial microseconds after impact. Propagation-based PCI offers sub-microsecond temporal resolution and the ability to obtain quantitative visualization of dynamic fracture processes in brittle materials. The setup consists of an in-line arrangement of an X-ray source, the sample, and an X-ray detector. The detector is not placed immediately behind the sample but at some known distance, so the radiation refracted by the sample can interfere with the unchanged beam. This leads to stronger contrast outlining the surfaces and structural boundaries of the sample (edge enhancement) compared with a conventional radiography. Because PCI relies on gradients in the phase of transmitted X-rays and the surface of a crack induces a steep gradient, the image contrast of cracks can be significantly enhanced compared to conventional radiography. Thus, PCI is particularly well-suited to imaging of cracks and dynamic failure phenomena.

Experimental triggering was done with 10-ns temporal resolution using the known standoff distance of the PZT pin from the target strike face and known cable delays. Mechanical and electronic shutters were used to synchronize to the impact event and isolate single synchrotron bunches in the 24-bunch mode of the APS (Jensen et al., 2013, 2014). A revolver undulator controls the beam mode used during the terminal event and was set to give a broadband white beam, which was ideal for doing phase contrast imaging. A single X-ray pulse beam was centered in time around a heat load chopper that opened during the shot so the beam could penetrate

the target during impact, project onto the scintillator, and be recorded by the detectors. The images were acquired on a four-frame camera, which took two images per frame (eight images total).

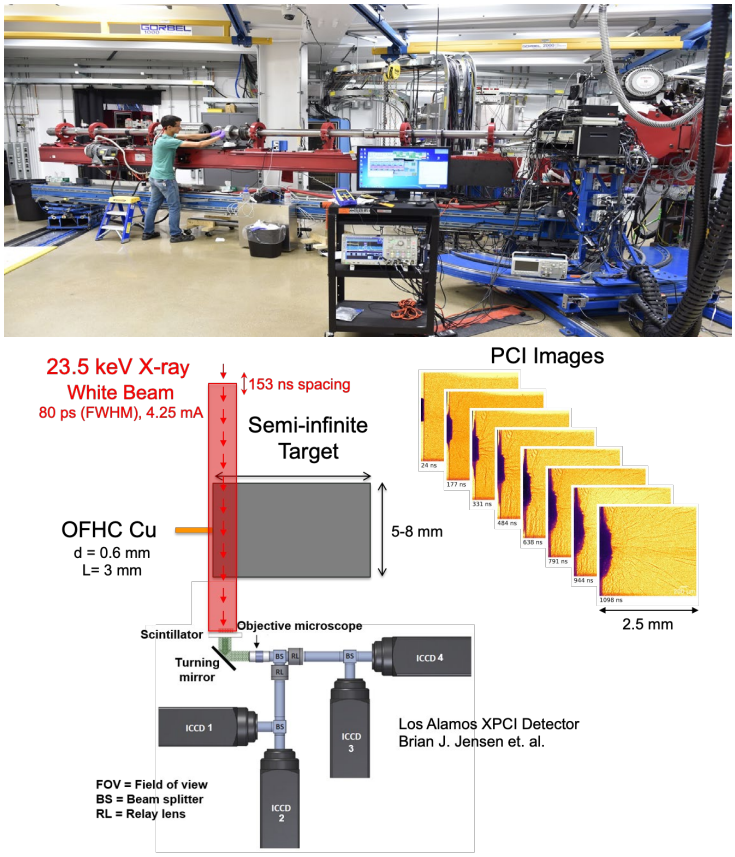

Fig. 1 Experimental setup for instrumented ballistic testing. (Top) Shown is one of the high-precision launchers capable of achieving 2.5 km/s for a single-stage powder gun. (Bottom) Schematic of the setup and data collected for phase contrast imaging experiments, which utilize optical triggers to synchronize X-ray pulses and instrumentation. Full motion control of the target and gun is possible with high linear and angular resolution for precise sample alignment (10 µm and 1 mrad, respectively).

2.2 Computer Vision Detection of Fracture

To generate a suitable image for statistical analysis, it is necessary to proceed from a black and white, grayscale, or even color image of the fracture to a binarized image in which only the cracks are represented. This can prove very challenging if the fracture surface does not contrast significantly with the background image either due to insufficient variation in light level or background noise. Noise can also result in false detections that are then treated as cracks in the final analysis. To minimize these sources of error, a series of filtering, contrast enhancement, and morphological operations are used both prior to and after binarization. This section outlines this process in detail using the case study of the X-ray images of boron

carbide from the experiment described in Section 2.1, as these represent a worst-case scenario in terms of difficulty of fracture detection. While the general steps will be applicable in any case, the specific details of the image analysis will change with image set and experimental setup. The details provided here are intended as a reference and example of how to detect cracks rather than a rigid recipe to be followed in every case.

The first step is to filter out image noise and take the complement of the image, inverting the dark and light areas. This is done to improve the performance of subsequent contrast enhancement and binarization steps. In this specific instance, an adaptive Weiner filter is used prior to calculating the image complement. Figure 2 shows the initial image and the filtered complement.

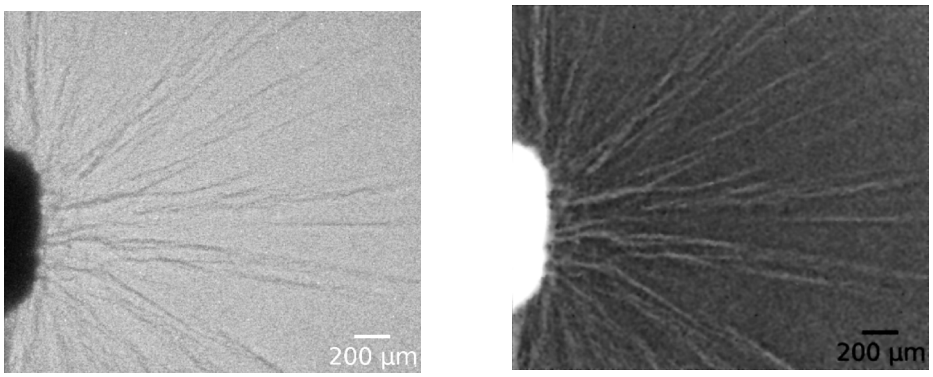

Fig. 2 (Left) The raw X-ray fracture image in boron carbide prior to any processing. (Right) The complement of the initial image after filtering out white noise.

Next, background illumination changes are subtracted from the image. This is important to ensure that the thresholds used in the binarization step are consistent across the entire image. To determine the background illumination, this example uses a morphological opening operation on the image using a square-shaped element with a size of 50 pixels. This effectively "smears" the image into overlapping squares of average coloration but is not well-suited to handling complex shapes like the scale bar, resulting in a region of significantly darker coloration that will cause problems in later analysis if not dealt with prior to subtraction from the main image. To deal with this issue, a nested loop is used to check each pixel of the background image and convert those with a grayscale intensity less than 40 to an intensity of 255, or bright white. The background illumination image is then subtracted from the main image. Figure 3 shows the background image and the processed main image. Note that in the main image, the scale bar is now removed.

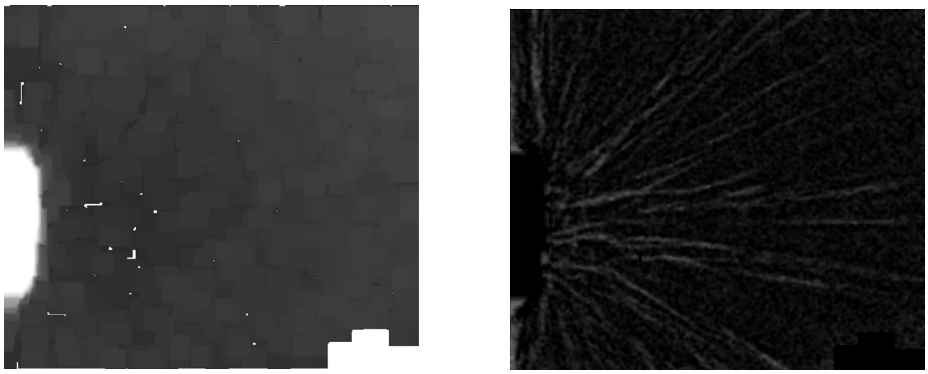

Fig. 3 (Left) The image used to determine background illumination differences. Note that the image is darker toward the left and lighter toward the right. (Right) The main image after the subtraction of the background illumination.

To convert the processed grayscale image into a binarized image suitable for analysis, a threshold value is selected. In this example pixels with a grayscale intensity greater than 17 were considered to be fractured and the remainder ignored, but this value is the most variable from experiment to experiment and is heavily dependent on the preprocessing as well. Figure 4 shows a montage from left to right, starting with the initial binarized image and proceeding through filtering steps. The first step filters out features with an area less than 60 pixels, getting rid of the smallest features resulting from noise. The second step further filters features with an area less than 200 pixels, followed by an image dilation then erosion using a small disk-shaped element. The two-step area filter is used for checking that the desired fracture elements are not being filtered along with the noise, as it is not uncommon for a crack to be represented by several small separated elements rather than one single element. The dilation/erosion step post-filtering helps to connect some of these disparate elements if they are sufficiently close by expanding to merge features together then contracting back to the original size everywhere except where features have connected. The final image in Fig. 4 shows the binarized image overlaid on the original fracture image. The cracks are detected with reasonable accuracy, but significant noise is still present.

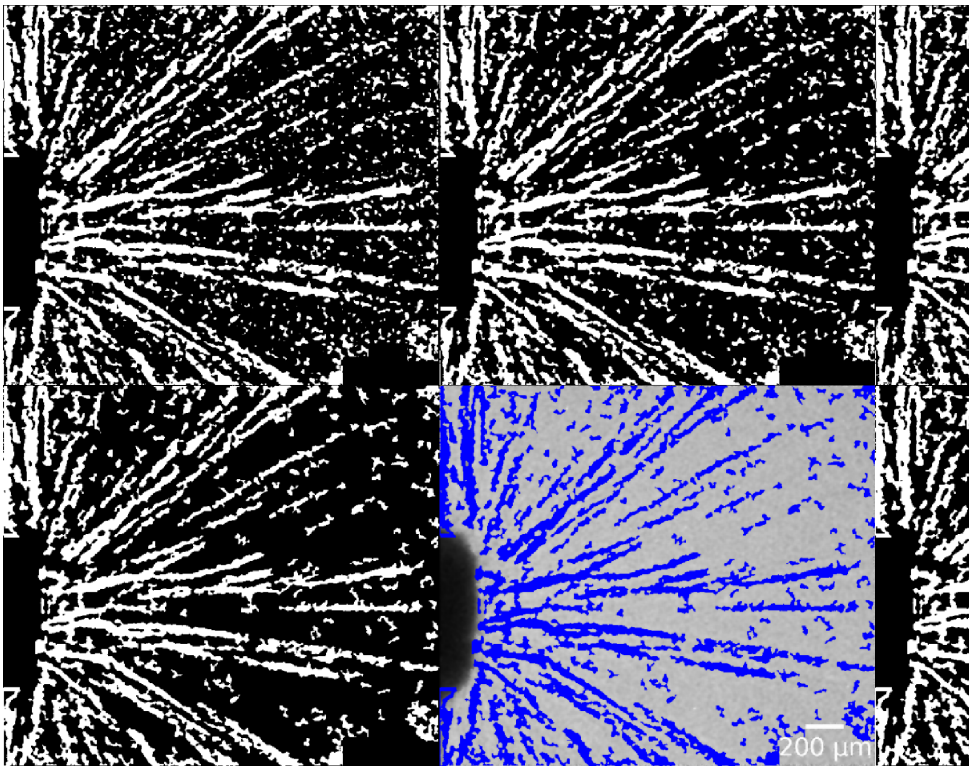

Fig. 4 (Top left) The initial binarized image is shown. Note both the detected cracks and extraneous noise. (Top right) The first filter step removes some of the noise but is not sufficient. (Bottom left) The second filter strep removes all but the largest noise features while leaving the cracks intact. (Bottom right) The final binarized image is overlaid on the original image.

The final step in the detection process is to skeletonize the binary image. This reduces each feature to a single pixel in width, with branches under a certain threshold length (in this example case, 30 pixels) trimmed to filter out false branches resulting from the nonuniform shape of the binarized image. The number and location of branch points can be determined from the skeletonized image. In some cases, it is first useful to fill in holes, or empty regions in the binarized image surrounded by filled regions, before calculating the branch points. This results in a less accurate determination of the crack location, but depending on the structure of the fracture, a more accurate determination of the branch points. This is true primarily for structures in the example, with radially branching cracks. If ring cracks around an impact site are present, this technique should not be used. Figure 5 shows both the skeletonized image used for the main analysis and a skeletonized image with the holes filled used to calculate the number of branches. The detected branch points are subtracted from the image, such that each remaining feature represents the length of a single crack from one end or branch point to the next. A final filtering step removes all features under 10 pixels in length. With the skeletonized image, it is now possible to extract statistics such as length and orientation.

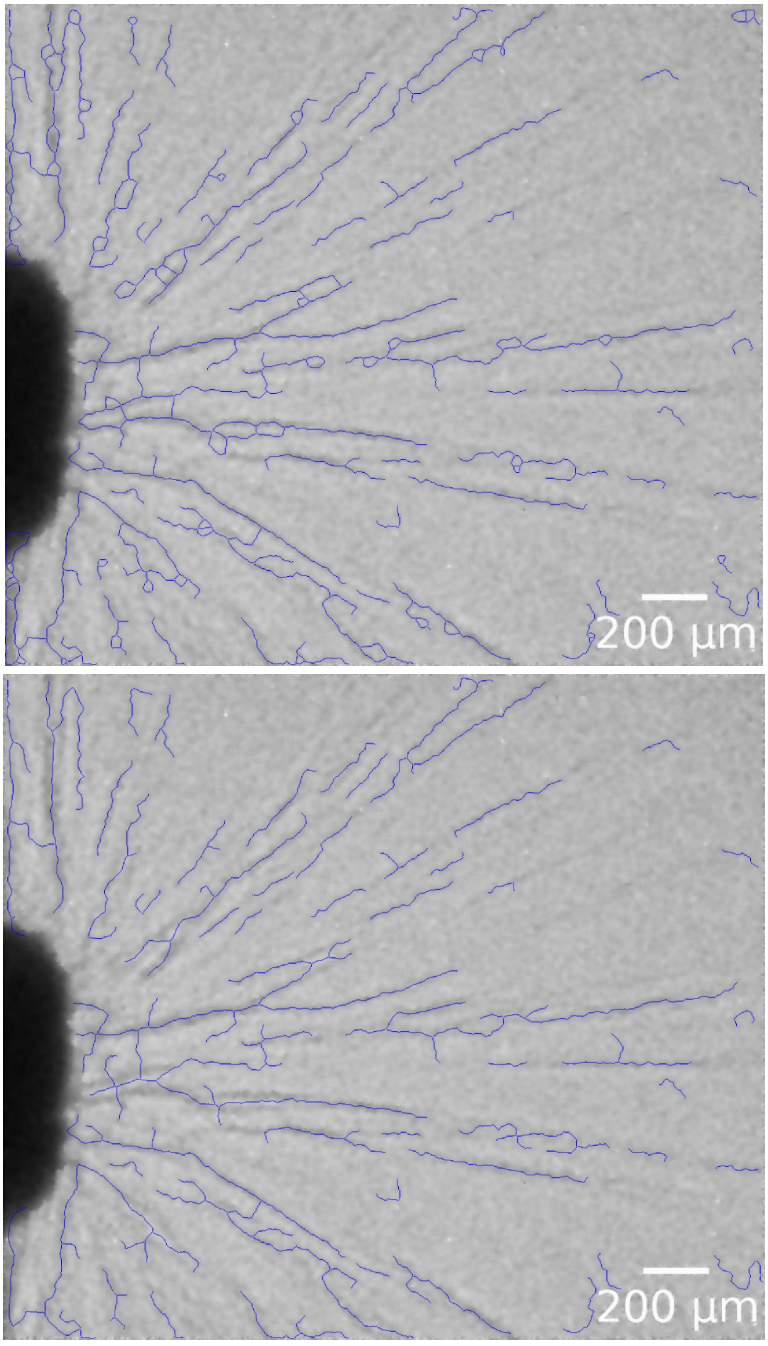

Fig. 5 (Top) The skeletonized image is shown. While cracks are mostly successfully detected, there remains some error, especially in the form of branched loops. (Bottom) A skeletonized version of the binarized image after a hole-filling operation is shown. This better captures the branching behavior at the cost of less accurate crack tracking, as can be seen near the impact site to the left.

3. Results and Discussion

3.1 X-ray Fracture in Boron Carbide

Figure 6 shows the fracture and penetration response for boron carbide when impacted at 1.9 km/s by a copper long rod. The images show massive failure due to axial and cone cracking. Typically, the only data that is extracted from this type of imaging includes depth of penetration as a function of time or qualitative assessment of the fracture morphology and severity. However, a wealth of information is transcribed in the extensive cracking and fragmentation that can detail the effects of both loading conditions as well as microstructure on the fracture evolution. This could provide invaluable insights into the underlying mechanics of brittle failure and aid in developing informed microstructure-property-performance relationships.

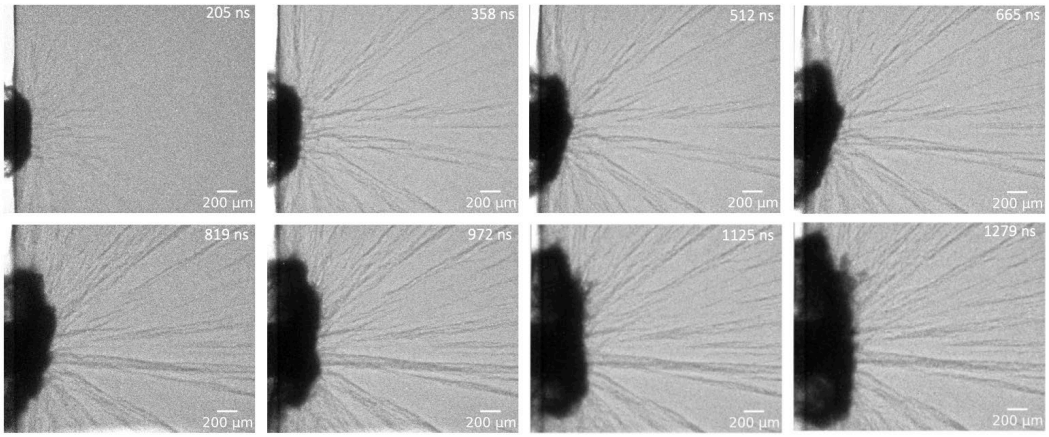

Fig. 6 All eight frames of the X-ray imagery of the fracture response of boron carbide

Using the methodology described in Section 2.2, it is possible to extract statistics from fracture images previously described only qualitatively. The mean length of the detected cracks shown in Fig. 5 was 106 µm, with a large standard deviation of 80 µm, showing that there was a wide distribution in crack lengths. The median crack length was 85 µm, and the total length of the detected crack system was 27.5 mm. Figure 7 presents this information in the form of a histogram of the crack distribution. The bulk of the detected cracks is under 150 µm, with a single outlier approximately 600 µm long. Figure 7 also shows the detected crack orientations. Orientations are calculated by taking the orientation of the major axis of an ellipse fit to the feature. The spread of orientations is relatively even, corresponding to the radial pattern observed visually in which the cracks observed range from straight up (90°) to straight down (–90°).

Tortuosity in this analysis is calculated as the measured length of each crack divided by the distance between the start and end pixel of each crack. In principle, this should always be at least one. However, it is possible to calculate lower tortuosity due to a combination of resolution and rounding issues. Crack length is measured by taking the total size, in pixels, of each detected and skeletonized feature. However, as pixels are square and eight-fold connectivity is used (connection on any of the four faces or along the four diagonals), it is possible to have a diagonal connection rounded to a length of two pixels when the actual length along the diagonal is 2.8 pixels. Future efforts will improve the method of determining tortuosity. Figure 7 shows the histogram of the measured tortuosity. The cracks in this experiment are mostly straight, radiating out from the impact site. Consequently, the tortuosity clusters around one, with a steadily decreasing distribution out to approximately three and a few outliers past that point, which likely come from erroneous detections.

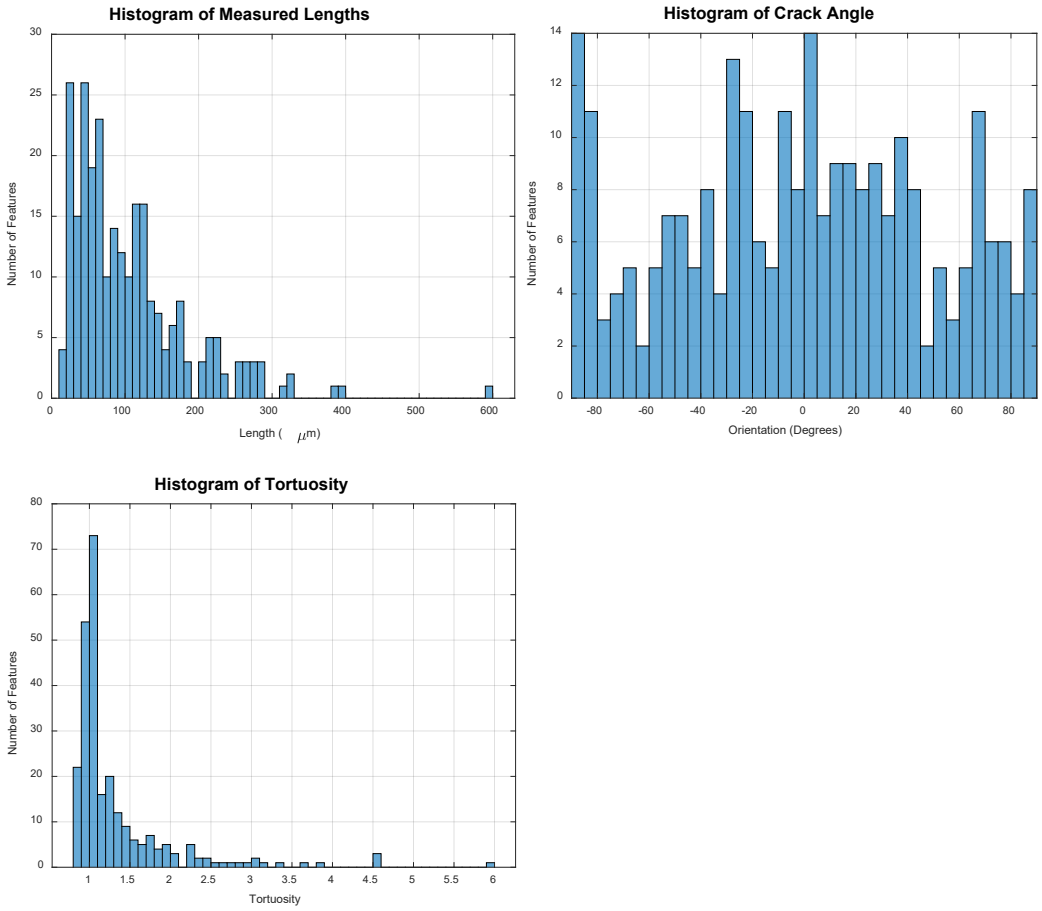

Fig. 7 (Top) The distribution of crack length is shown. Cracks under 10 µm are removed to filter noise. Most cracks are between 10 and 150 µm in length, with one outlier of approximately 600 µm. (Middle) The orientation of each crack is shown. The spread is relatively even, corresponding with the visually observed radial spread of fracture from the impact location. (Bottom) A histogram of the calculated tortuosity is shown. As most of the cracks in the analyzed image are straight, the tortuosity clusters around a value of one.

Table 1 shows the collected statistics for frames 2–8 of the X-ray experiment. Frame 1 is omitted, as there is not sufficient fracture to analyze. Several conclusions can be drawn as to the behavior of the sample and propagation of fracture over time. The various measurements of length, barring a few outliers that show up for a single frame, are mostly consistent. This suggests that the measured cracks do not change much over the course of the experiment—a somewhat surprising conclusion, but one supported by a qualitative study of the imagery in which the majority of the cracks visible form between frame 1 (which is mostly unfractured) and frame 2. While there is some additional crack growth, it is small compared to the amount present from the beginning of the analysis and seems to be below the floor of the error in the visual detection. The orientation measurements provide insight into the angular spread of the fracture. With maximum and minimum values at the full range of +/–90°, as well as mean and median values near zero and a large standard deviation, it is clear that there is no preferential orientation in any frame. As shown in the in-depth analysis of frame 2, this represents a conical spread from the impact location. The tortuosity gives an overview of the straightness of the fractures. While there is a clear increasing trend in the maximum value, the mean and median values remain consistent, suggesting that the majority of detected crack features cluster around a tortuosity value of one and are mostly straight. The outlier maximum values likely arise from either an erroneous detection or fractures ahead of the expanding failure zone at the point of impact.

Table 1 Collected statistics

	Frame 2	Frame 3	Frame 4	Frame 5	Frame 6	Frame 7	Frame 8
Length (µm)							
Max	596	584	537	510	848	607	481
Min	19.4	19.4	19.4	19.4	19.4	21.3	19.4
Mean	106	117	98.8	85.8	110	126	97.8
St. Dev	80.2	96.7	88.6	69.6	93.3	106	75.8
Median	85.4	83.4	66.0	64.0	83.42	95.1	74.7
Total	27480	25808	28749	41597	31331	27358	30311
Orientation							
Max	90.0	89.3	89.9	90	90	89.3	89.7
Min	–89.8	–78.7	–88.7	–88.7	–89.8	–88.7	–89.1
Mean	–1.56	5.35	3.45	4.53	2.27	10.7	4.89
St. Dev	50.1	49.2	45.2	47.6	41.0	38.2	41.5
Median	0.22	3.79	3.40	4.80	4.74	9.81	6.04
Tortuosity							
Max	6.00	7.39	8.49	11.3	5.63	12.0	14.1
Min	0.813	0.828	0.785	0.766	0.804	0.812	0.799
Mean	1.33	1.38	1.29	1.35	1.20	1.29	1.33
St. Dev	0.689	0.868	0.797	0.94	0.516	0.910	1.12
Median	1.06	1.04	1.03	1.05	1.02	1.03	1.03
Branch Points	147	104	128	233	146	105	157

Finally, while the branch points have been collected for each frame, the number varies significantly and without a clear trend. This value is heavily affected by the number of smaller features detected, whether due to actual branching or noise, and in this case the error in the analysis appears to be larger than any variation in branch points. Measurement of branch points will have more significance for smaller, better-defined crack networks.

3.2 Randomized Behind-Helmet Blunt Trauma Simulations

Alexander et al. (2021) developed an improved methodology to study failure and fracture during skullcap injuries. This improvement included a technique to randomize element properties while keeping the original mesh, simulating biovariability in human bones and allowing for the generation of several similar but distinct fracture patterns. Figure 8 shows the results of this technique, with an initial mesh and five simulations run on a randomized version. This large data set provides an opportunity for developing a statistical profile of the "average" fracture for the studied loading conditions and skull properties. A statistical profile of this type has several potential uses. The first is to validate the randomized fracture profiles by comparing them to the original, providing additional insight into the influence of internal porous structures in the bone which are *not* currently included in the randomization method. The second use is to validate the model itself against experimental data. The latter is particularly useful as fracture is highly dependent on the random distribution of microstructural elements and flaws. A statistical profile of multiple experiments or simulations represents a more accurate comparison than a single case.

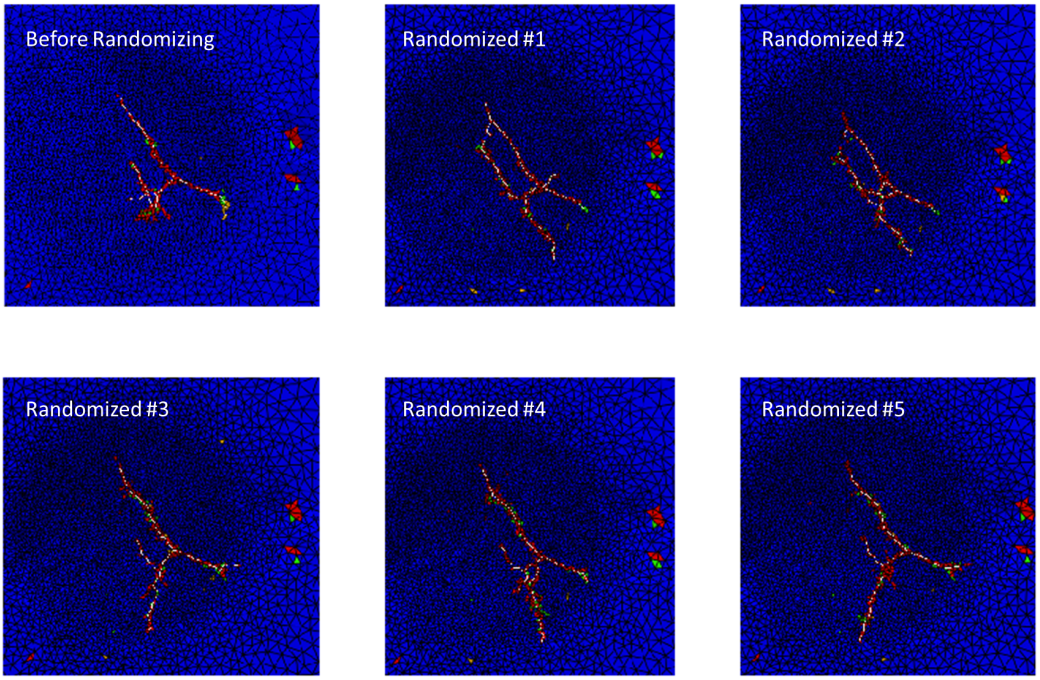

Fig. 8 Simulations of fracture in a model skull are overlayed with detected cracks (white lines). The blue elements are undamaged, while other colors represent failed elements that make up simulated cracks. The top-right image uses the initial simulation parameters, while the remainder use randomized element properties to mimic the variability of human bone.

Table 2 presents a limited statistical profile of the model results depicted in Fig. 8. Only lengths are studied here for the sake of brevity, though the other measures used in the previous case studies could be extracted if determined to be useful. Additionally, the better accuracy due to the lack of noise in the model compared to the X-ray images allows for the extraction of a count of the number of branches. The extracted data reveals several points of comparison between the initial model and the randomized cases. The maximum crack length in the initial model is higher than any of the simulated cases, raising the possibility that something about the randomization process causes shorter cracks or greater branching. The measurement of the branches disproves the last possibility, however, showing that the number of branching points in the initial model is within the range found in the randomized models. The minimum crack length is smaller for the randomized simulations in all but one case as well, though the average crack length is similar. The standard deviation of the crack lengths for the initial case is again higher than the randomized cases, with the randomized case 5 coming the closest to the initial case in both the standard deviation and maximum crack length.

Table 2 Skullcap fracture simulations

	Before randomization	Random 1	Random 2	Random 3	Random 4	Random 5	Mean
Length (px)							
Max	252	117	119	186	164	234	179
Min	22	21	15	34	11	10	18
Mean	70.8	59.3	50.3	74.5	62.8	77.7	65.9
St. dev.	89.8	41.3	39.5	58.7	54.6	84.7	61.4
Median	32.5	31.0	31.5	56.0	53.5	49.5	52.33
Total	425	534	503	447	502	466	480
No. of branches	5	4	4	6	4	5	4.6

Finally, the total length of the initial case is lower than any of the randomized cases. The takeaway from this comparison is that the initial case has a long unbranched crack that the randomized cases do not. Instead, the randomized cases tend to have a more even distribution of crack sizes. If enough experimental results with a comparable loading condition were available, similar statistics could be extracted to see if the difference between the initial case and the randomized cases is meaningful, as well as how accurately the simulations as a whole agreed with the fracture behavior observed experimentally.

4. Conclusions

Detection and analysis of images of complex fractures allow for the quantification of data previously only useful for qualitative study. Numerical comparison between experiments, or between experimental data and modeling, greatly increases the density of information extracted from high-speed imagery and presents a method of studying complex interacting cracks that cannot be captured with traditional fracture experiments. The method presented in this report is still under active development. Several opportunities exist to improve on the results shown in the two case studies. The first and largest area of improvement is in the detection of cracks. The current method uses computer vision techniques to filter noise and enhance contrast. However, machine learning techniques offer the potential for quicker, more accurate, and less labor-intensive crack detection in the future. Additionally, the statistical data presented here only scratches the surface of what could be extracted. Future work will measure quantities such as total lengths within given bands of crack orientation and the spacing, both in total distance and angular, between adjacent cracks. A complete statistical depiction of the geometrical relationship between cracks will both tease out nonobvious fracture behavior from individual experiments and also allow for more accurate comparisons between experiments and simulations.

5. References

Alexander SL, Baumer T, Fagan B, Weerasooriya T. Hybrid experimental modeling computational (HEMC) skullcap simulation: elemental to layer simplification and application to microstructural stochasticity. DEVCOM Army Research Laboratory (US); 2021. Report No.: ARL-TR-9125.

Dally JW, Kobayashi T. Dynamic photoelastic determination of the a-K relation for 4340 alloy steel. ASTM International; 1980.

Jensen BJ, Owens CT, Ramos KJ, Yeager JD, Saavedra RA, Iverson AJ, Luo SN, Fezzaa K, Hooks DE. Impact system for ultrafast synchrotron experiments. Rev Sci Instrum. 2013;84(1):013904.

Jensen BJ, Ramos KJ, Iverson AJ, Bernier J, Carlson CA, Yeager JD, Fezzaa K, Hooks DE. Dynamic experiment using impulse at the advanced photon source. J Phys Conf Ser. 2014;500(4):042001. IOP Publishing.

Kirugulige M, Tippur H, Denney T. Investigation of mixed-mode dynamic fracture in syntactic foams using digital image correlation method and high-speed photography. Proceedings 2007 SEM Annual Conference Exposition Experimental Applied Mechanics; 2007.

Periasamy C, Tippur HV. Full-field digital gradient sensing method for evaluating stress gradients in transparent solids. Appl Opt. 2012;51(12):2088–2097.

Shannahan L. A hybrid experimental-computational approach for the analysis of dynamic fracture [dissertation]. Drexel University; 2017.

Shannahan L, Barsoum MW, Lamberson L. Dynamic fracture behavior of a MAX phase Ti3SiC2. Eng Fract Mech. 2017;169:54–66.

Shannahan L, Weerasooriya T, Gunnarsson A, Sanborn B, Lamberson L. Rate-dependent fracture modes in human femoral cortical bone. Int J Fract. 2015;194(2):81–92.

Yoneyama S, Morimoto Y, Takashi M. Automatic evaluation of mixed-mode stress intensity factors utilizing digital image correlation. Strain. 2006;42(1):21–29.

Zehnder AT, Rosakis AJ. Dynamic fracture initiation and propagation in 4340 steel under impact loading. Int J Fract. 1990;43(4):271–285.

List of Symbols, Abbreviations, and Acronyms

APS	Advanced Photon Source
B_4C	boron carbide
DIC	digital image correlation
PCI	phase contrast imaging

1 (PDF)	DEFENSE TECHNICAL INFORMATION CTR DTIC OCA
1 (PDF)	DEVCOM ARL FCDD RLD DCI TECH LIB
2 (PDF)	DEVCOM ARL FCDD RLW TB L SHANNAHAN FCDD RLW TF P JANNOTTI